

# Determination of helix orientations in a flexible DNA by multi-frequency EPR spectroscopy

C. M. Grytz,<sup>a,b,†</sup> S. Kazemi,<sup>b,c,d,†</sup> A. Marko,<sup>a,b</sup> P. Cekan,<sup>e</sup> P. Güntert,<sup>b,c,f,g</sup>  
S. Th. Sigurdsson<sup>\*,e</sup> and T. F. Prisner<sup>\*,a,b</sup>

- 
- <sup>a.</sup> Institute of Physical and Theoretical Chemistry, Goethe University, Max-von-Laue-Str. 7, 60438 Frankfurt am Main, Germany.
- <sup>b.</sup> Center of Biomolecular Magnetic Resonance, Goethe University, Max-von-Laue-Str. 9, 60438 Frankfurt am Main, Germany.
- <sup>c.</sup> Institute of Biophysical Chemistry, Goethe University, Max-von-Laue-Str. 9, 60438 Frankfurt am Main, Germany.
- <sup>d.</sup> Frankfurt Institute for Advanced Studies, Ruth-Moufang-Str. 1, 60438 Frankfurt am Main, Germany
- <sup>e.</sup> University of Iceland, Department of Chemistry, Science Institute, Dunhaga 3, 107 Reykjavik, Iceland
- <sup>f.</sup> Laboratory of Physical Chemistry, ETH Zürich, Vladimir-Prelog-Weg 2, 8093 Zürich, Switzerland
- <sup>g.</sup> Graduate School of Science, Tokyo Metropolitan University, 1-1 Minami-ohsawa, Hachioji, Tokyo 192-0397, Japan

## Table of Contents

1	Thermal denaturation experiments	2
2	Experimental details	2
2.1	Continuous-wave EPR at X-band frequencies .....	2
2.2	PELDOR at X-, Q- and G-band frequencies .....	4
2.2.1	Reproducibility of the modulation depth	5
3	Original experimental PELDOR time traces	7
4	Data analysis with respect to distance distribution	8
5	Simulations and fit to the experimental PELDOR data	8
5.1	PELDOR data simulation.....	8
5.2	Details to structure calculations .....	8
5.3	Details about the EPR/NMR-based approach for ensemble determination .....	9
5.4	Determination of a structural ensemble using a geometric model and PELDOR data ..	11
5.5	Calculation of the helix axis.....	14
5.6	Prediction of high-field PELDOR data .....	14
5.7	Simultaneous fit to all experimental PELDOR data .....	16
6	References	18

## 1 Thermal denaturation experiments

Thermal denaturation experiments were performed for proving non-strand dissociation and stability of the secondary structure of the unlabeled and the three labeled bent DNA mutants. The temperature of half-dissociation of the DNA duplex, called the melting temperature ( $T_m$ ), was obtained from the maximum of the first derivative  $dA/dT$  graphs (where  $A$  is the absorbance and  $T$  is the temperature). A melting temperature lower than 3.5 °C the unmodified DNA was observed for the mutants.

**Table S1.** Melting temperatures  $T_m$  for the unmodified bent DNA and the three modified bent DNA samples. Deviation of the melting temperatures  $T_m$  of the modified DNAs relative to the unmodified DNA ( $\Delta T_m$ ).

Sample	Sequence	$T_m$ [°C]	$\Delta T_m$ [°C]
Non-modified DNA	5'-GCA TCG AAA AAG CTA CG + 3'- CGT AGC-----C GAT GC	$32.5 \pm 0.5$	
DNA5,16	5'-GCA TCG AAA AAG CTA CG + 3'- CGT AGC-----C GAT GC	$30.7 \pm 0.7$	-1.8
DNA2,13	5'-GCA TCG AAA AAG CTA CG + 3'- CGT AGC-----C GAT GC	$29.0 \pm 1.0$	-3.5
DNA2,16	5'-GCA TCG AAA AAG CTA CG + 3'- CGT AGC-----C GAT GC	$31.3 \pm 0.3$	-1.2

## 2 Experimental details

### 2.1 Continuous-wave EPR at X-band frequencies

For the X-band CW-EPR spectra, a volume of 20  $\mu$ L of the samples were filled in an EPR tube (2 mm OD). The spectra were recorded on a Bruker Elexsys-500 X-band spectrometer equipped with a standard rectangular (ER4102ST7934) cavity at room temperature. The microwave frequency was determined using a Systron Donner (6054D frequency counter). The magnetic field was measured with a Bruker Gaussmeter (ER035M). The experimental parameters were set at 100 kHz modulation frequency, 1 G modulation amplitude, 1 mW microwave power, 40.96 ms time constant, 40.96 ms conversion time and 41.96 ms sweep time. The magnetic field was swept from 3218 G to 3498 G with a center field of 3358 G. The resolution was 1024 data points.

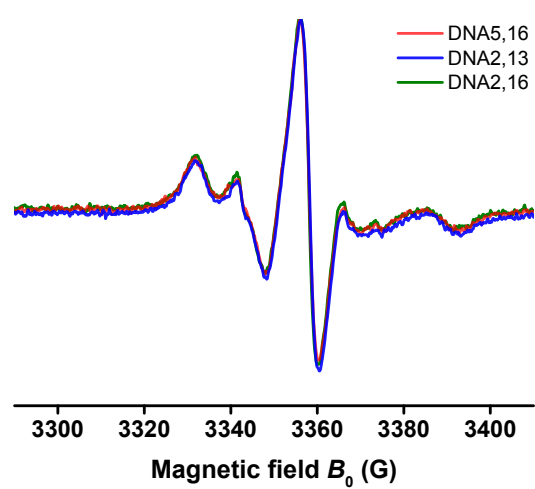


**Fig. S1** CW-EPR spectra recorded at room temperature of all measured DNA samples.

## 2.2 PELDOR at X-, Q- and G-band frequencies

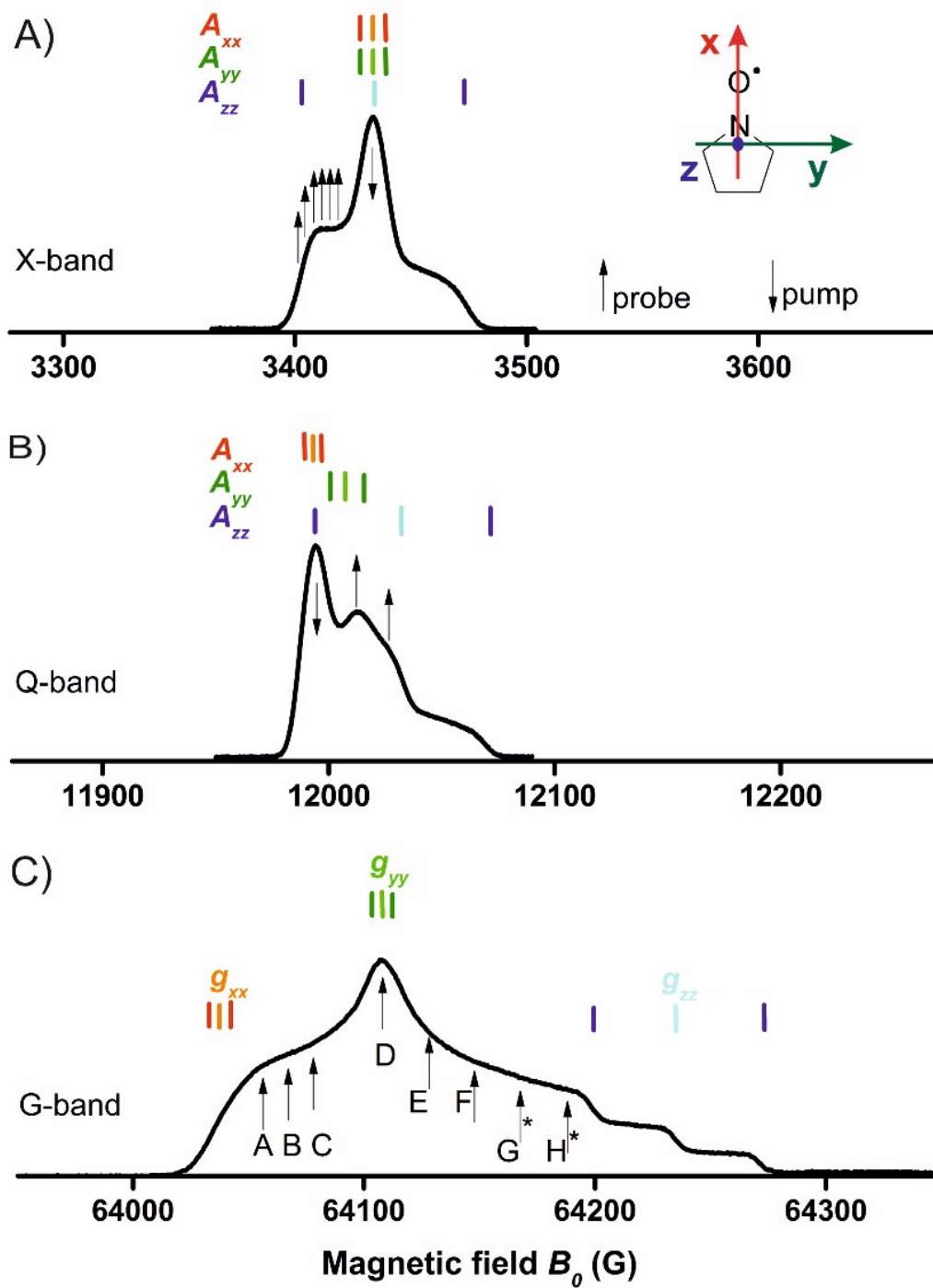


**Fig. S2** Echo-detected field swept EPR spectra of  $^{15}\text{N}$ -spin labeled bent DNA recorded at 40 K and corresponding  $^{15}\text{N}$  stick diagram for (A) X-, (B) Q- and (C) G-band frequencies, respectively. Arrows indicate pump and probe frequencies with varied detection positions  $\Delta\nu$  ranging from 40 to 90 MHz at X-band frequencies. At Q-band frequencies the pump pulse was set to the maximum absorption position and the probe pulses 50 and 90 MHz below. At G-band frequencies, arrows mark the detection positions. The pump frequency was set at a constant offset  $\Delta\nu$  of 60 MHz below or above (positions G and H marked with \*) the detection frequency. The magnetic field was not calibrated.

### 2.2.1 Reproducibility of the modulation depth

In order to demonstrate the variance in the modulation depth from experiment to experiment of the PELDOR time traces recorded at G-band frequencies, we obtained experimental independently recorded PELDOR time traces. For each measurement the same experimental parameters were used. Two different positions were measured: First, the detection was set at the maximum of the nitroxide spectra (position D in Fig. S2C, Fig. S3A). Second, the magnetic field position was set half way between the low field edge and the maximum of the EPR spectra (position C in Fig. S2C, Fig. S3B). As can be seen in Fig. S3 the shapes of the PELDOR time traces are identical within the signal to noise whereas the modulation depths vary from experiment to experiment.

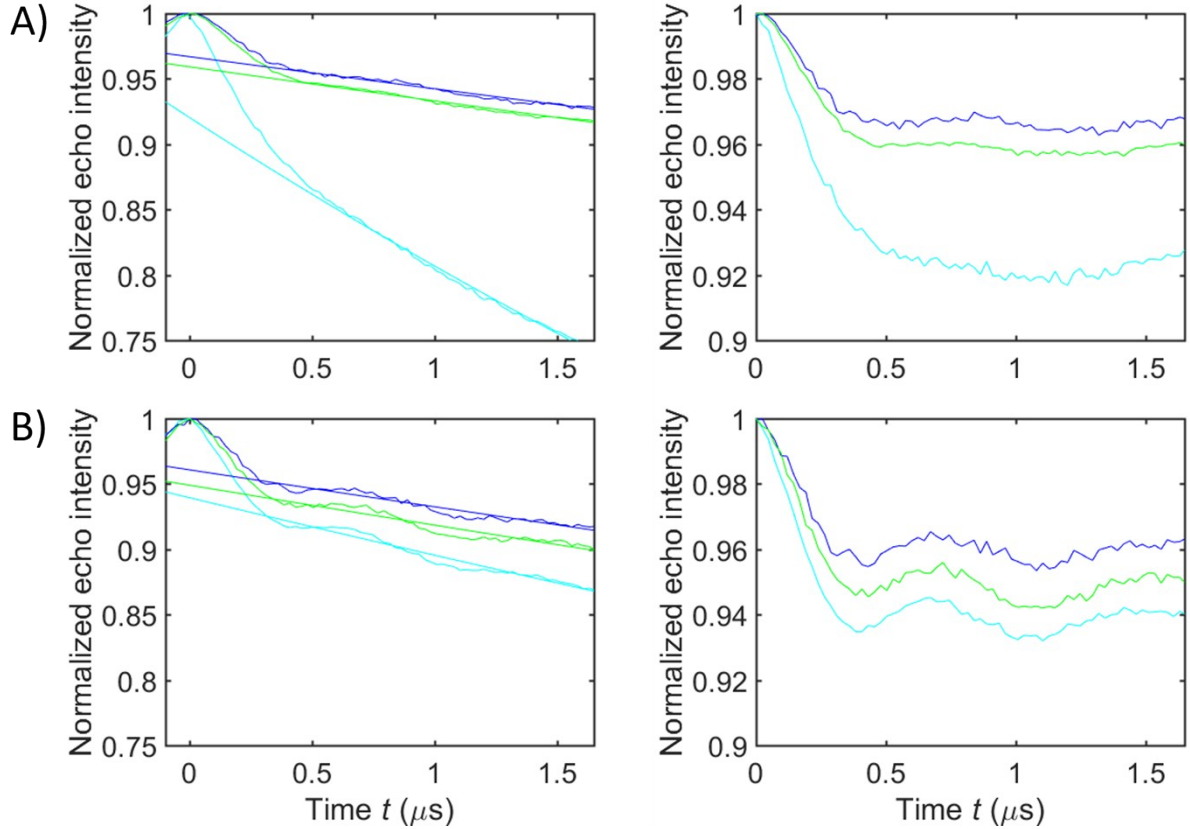


**Fig. S3** (A) Left: Experimental PELDOR time traces measured at the maximum of the nitroxide spectra (position D in Fig. S2) and the corresponding background function of **DNA2,13**. Right: Experimental background-divided PELDOR time traces. (B) Left: Experimental PELDOR time traces measured -30 G away from the maximum of the nitroxide spectra (position C in Fig. S2) and the corresponding background function of **DNA2,13**. Right: Experimental background-divided PELDOR time traces.

For the calculation of the reproducibility of the modulation depth parameter  $\lambda$ , we used the Student's  $t$ -distribution. The  $t$ -coefficient  $t_{\alpha,v}$  with the degree of freedom  $v = n - 1$  ( $n$  number of measurement values) and the probability  $1 - \alpha$ , that the true measurement value will be less than  $t_{\alpha,v}$ , can be taken from a  $t$ -distribution quantiles table. In this study, we repeated the

measurements 3 times resulting in  $\nu = 2$ . The errors were calculated with a 95% confidence. Therefore, the  $t$ -coefficient was  $t_{0.95,2} = 2.92$ . The confidence interval for the mean modulation depth parameter  $\lambda$  was calculated by using the formula  $\bar{\lambda} \pm t_{\alpha,\nu} \frac{\sigma_{\lambda}}{\sqrt{n}}$ . At 95% confidence, the true modulation depth parameter  $\lambda$  is expected to be within  $\lambda_1 = 0.005 \pm 0.0037$  (74%) (Fig. S3A) and  $\lambda_2 = 0.0049 \pm 0.0019$  (39%) (Fig. S3B).

**Table S2.** Error estimation of the modulation depth parameter. Mean value  $\bar{\lambda}$  and standard deviation  $\sigma_{\lambda}$  with its percentage amount, mean value  $\bar{\lambda}$  and standard deviation under use of a Student's  $t$ -distribution.

time traces recorded at	$\bar{\lambda} \pm \sigma_{\lambda}$	$\sigma_{\lambda} / \bar{\lambda} (\%)$	$\bar{\lambda} \pm t_{0.95,2} \frac{\sigma_{\lambda}}{\sqrt{3}}$	$t_{0.95,2} \frac{S_3}{\sqrt{3}} / \bar{\lambda} (\%)$
position D in Fig. S2C	$0.0050 \pm 0.0022$	44	$0.0050 \pm 0.0037$	74
position C in Fig. S2C	$0.0049 \pm 0.0011$	22	$0.0049 \pm 0.0019$	39

In summary, the reproducibility of the modulation depth is within 39–74% with a confidence of 95% using Student's  $t$ -distribution (further information can be found in the Supporting Information, Fig. S3). This is due to variations in the experimental conditions. The  $B_1$ -Field was not always consistent and reproducible.

### 3 Original experimental PELDOR time traces

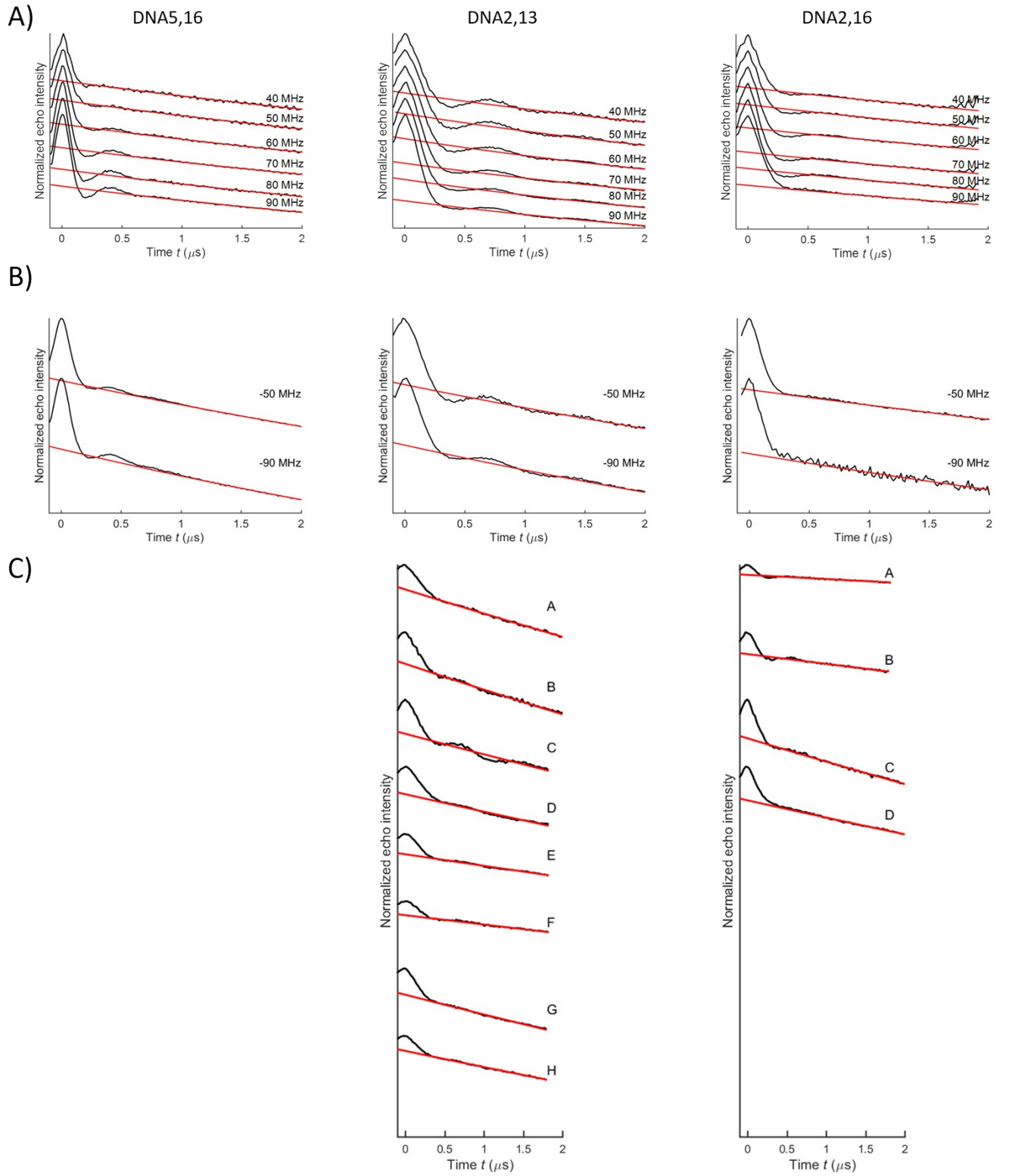


**Fig. S4** Experimental PELDOR time traces measured at frequency offsets  $\Delta\nu$  from 40 to 90 MHz at (A) X-, (B) Q- and (C) G-band frequencies for all spin-labeled DNAs. The background function is shown in red. The field positions A-H are marked in Fig. S2C.

## 4 Data analysis with respect to distance distribution

For distance determinations, a single time trace with reduced influence of orientation effects was generated by summing up the X-band PELDOR time traces over all measured frequency offsets  $\Delta\nu$ .<sup>1-2</sup> Prior to summing up, an exponential background was fitted to the last 2/3 of the PELDOR time traces and the PELDOR trace was then divided by this background function using the software DeerAnalysis2011<sup>3</sup> and DeerAnalysis2013 for the time traces recorded at X- and Q-band and at G-band frequencies, respectively. Data points at the end of the time trace were cut off to avoid artefacts at  $t_{\max}$  caused by the overlap between the pump pulse and the second  $\pi$ -pulse of the probe-channel. Distribution functions of the distance  $R$  connecting the two  $\text{C}$  spin labels for all DNA samples were obtained from the averaged time traces using DeerAnalysis with a Tikhonov regularization<sup>4</sup>. The L-curve criterion was applied to estimate the optimal regularization parameter  $\alpha$ , which was set to 100.

## 5 Simulations and fit to the experimental PELDOR data

### 5.1 PELDOR data simulation

For PELDOR data simulation, the following magnetic parameters were used for both nitroxides:

$g$ -tensor:  $g_{xx} = 2.0090$ ,  $g_{yy} = 2.0066$ ,  $g_{zz} = 2.0027$

$A$ -tensor:  $A_{xx} = 5$  G,  $A_{yy} = 5$  G,  $A_{zz} = 36$  G

The line broadening was set to 4.7 G. The pulse lengths, flip angles, magnetic field positions, pump and probe frequencies were chosen the same as in the experiment. All equations necessary for PELDOR data simulation can be found in the following references.<sup>2, 5-7</sup>

### 5.2 Details to structure calculations

Fig. S5 shows the CYANA target function values from individual structure calculations as a function of the systematically varied PELDOR spin-spin distance restraint. This demonstrates that only extreme distance bounds for the PELDOR distance restraints lead to a significant rise of the CYANA target function.



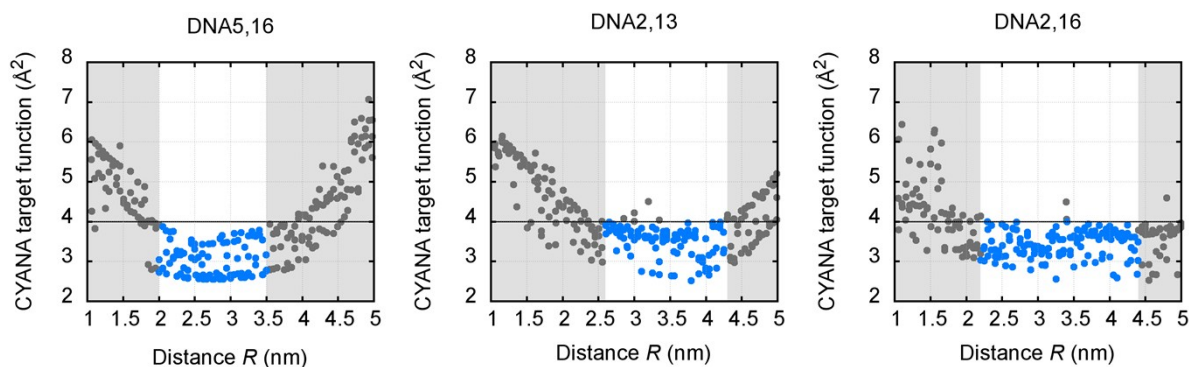


**Fig. S5** CYANA target function values plotted as a function of the spin-spin distance between the  $C$  spin labels for the three DNA sample. The other distance restraints were as in the original NMR structure. The black line at  $4 \text{ Å}^2$  indicates the target function cutoff for accepted structures based on NMR. All structures in very good agreement with the NMR data (blue) were within the corresponding PELDOR distance range (white) and under the target function value of  $4 \text{ Å}^2$ .

### 5.3 Details about the EPR/NMR-based approach for ensemble determination

Fig. 4A in the paper shows the fit to the experimental PELDOR time traces at X-band frequencies obtained by the combined EPR/NMR approach. There the modulation depth of the PELDOR traces for  $2.0 \mu\text{s}$  of the simulation has been adjusted to the experimental trace for better comparison. In Fig. S6 the modulation depths were not adjusted.

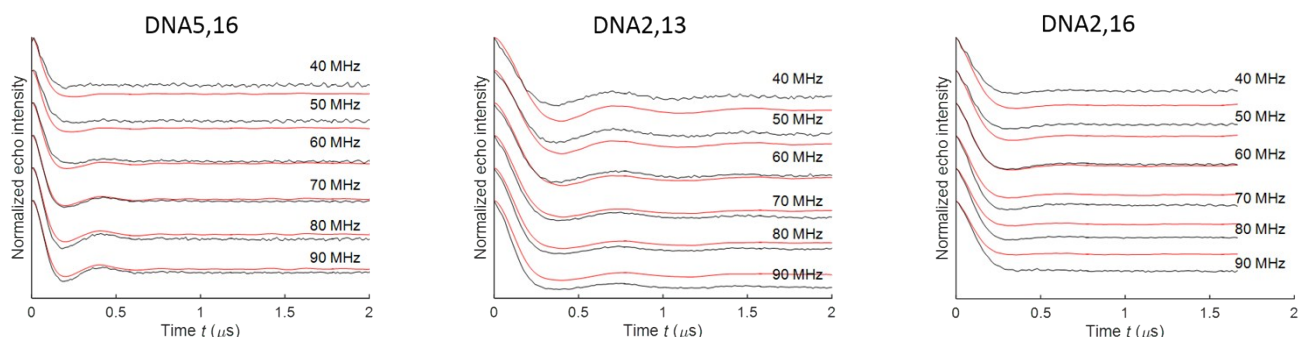


**Fig. S6** Comparison of experimental (black) and fitted (red) X-band PELDOR time traces for different frequency offsets  $\Delta\nu$  for **DNA5,16**, **DNA2,13** and **DNA2,16**. Fitted PELDOR time traces were obtained by the combined NMR/EPR approach for ensemble determination. The modulation depth of the PELDOR traces for  $2.0 \mu\text{s}$  of the simulations was not adjusted to the experimental trace.

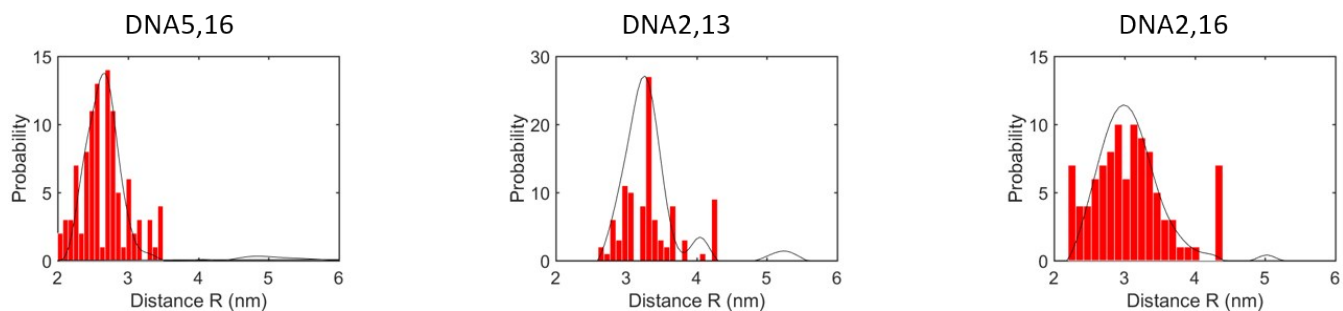


**Fig. S7** Simulation of distance distributions based on a Tikhonov regularization of the X-band PELDOR data averaged over all measured frequency offsets  $\Delta\nu$  (black line) and back-calculated distance distribution of the structural bundle found by the EPR/NMR approach, shown in red. The experimental distance distributions were scaled to the maximum of the histogram obtained by the NMR structures.

During the fitting procedure, the deviation from the selected pre-simulated time traces (according to equation 2) reduces drastically after a few iteration steps (Fig. S8) resulting in a low deviation from the experimental data.

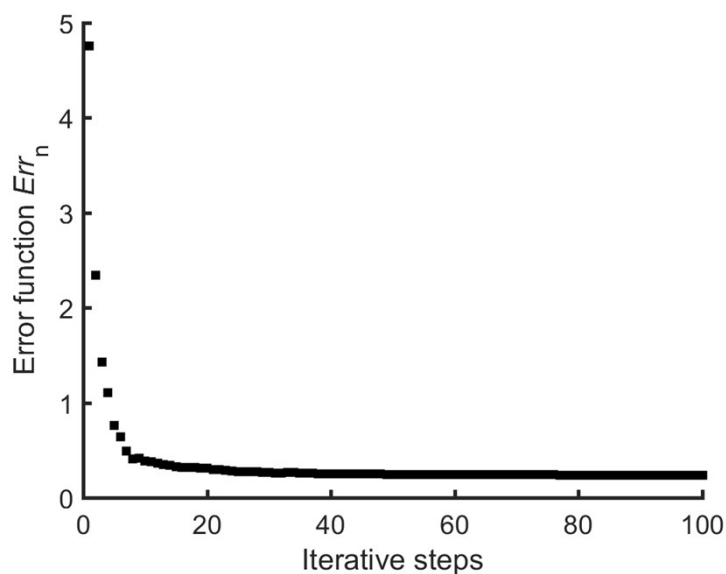


**Fig. S8** Deviation between the sum of selected pre-simulated time traces and the experimental X-band frequencies PELDOR time traces after each iteration step.

#### **5.4 Determination of a structural ensemble using a geometric model and PELDOR data**

In principle, a library of possible conformers can be generated without the NMR data. Therefore, we compared the fitting results using the library generated with NMR data and the library without the NMR data.

When fitting the X-band PELDOR data sets without the NMR restraints we used a simple geometric model (Fig. S9). The model consists of two rigid helices linked by an on-axis hinge with a variable distance from the helix. Fig. 5 shows that the conformational space obtained by this procedure differs from the one obtained by including the NMR data despite the fact that both approaches identify the most populated conformers. Specifically, we observe structures with twist angles (Fig. S10) below  $180^\circ$  when omitting the NMR data. However, these twist angles are located outside the allowed region of the structural library (Fig. 5B). Thus, these structures are not in agreement with the NMR data and PELDOR distance regions, indicating that they probably contains non-native structures.

This result can be rationalized because the solution obtained with the EPR and NMR restraints contains conformers where the two double-helical axis do not cross, in contrast to the model with PELDOR restraints only. This is consistent with a somewhat lower quality of the fit of the time domain PELDOR sets when the NMR data is omitted (Fig. S9). Fitting without any additional restraints would give perfect fits but include physical impossible arrangements between the two helices. Of course, more elaborate models of the molecule could be used for fitting, but we believe that our approach, based on experimental data from NMR and PELDOR is superior to such approaches.

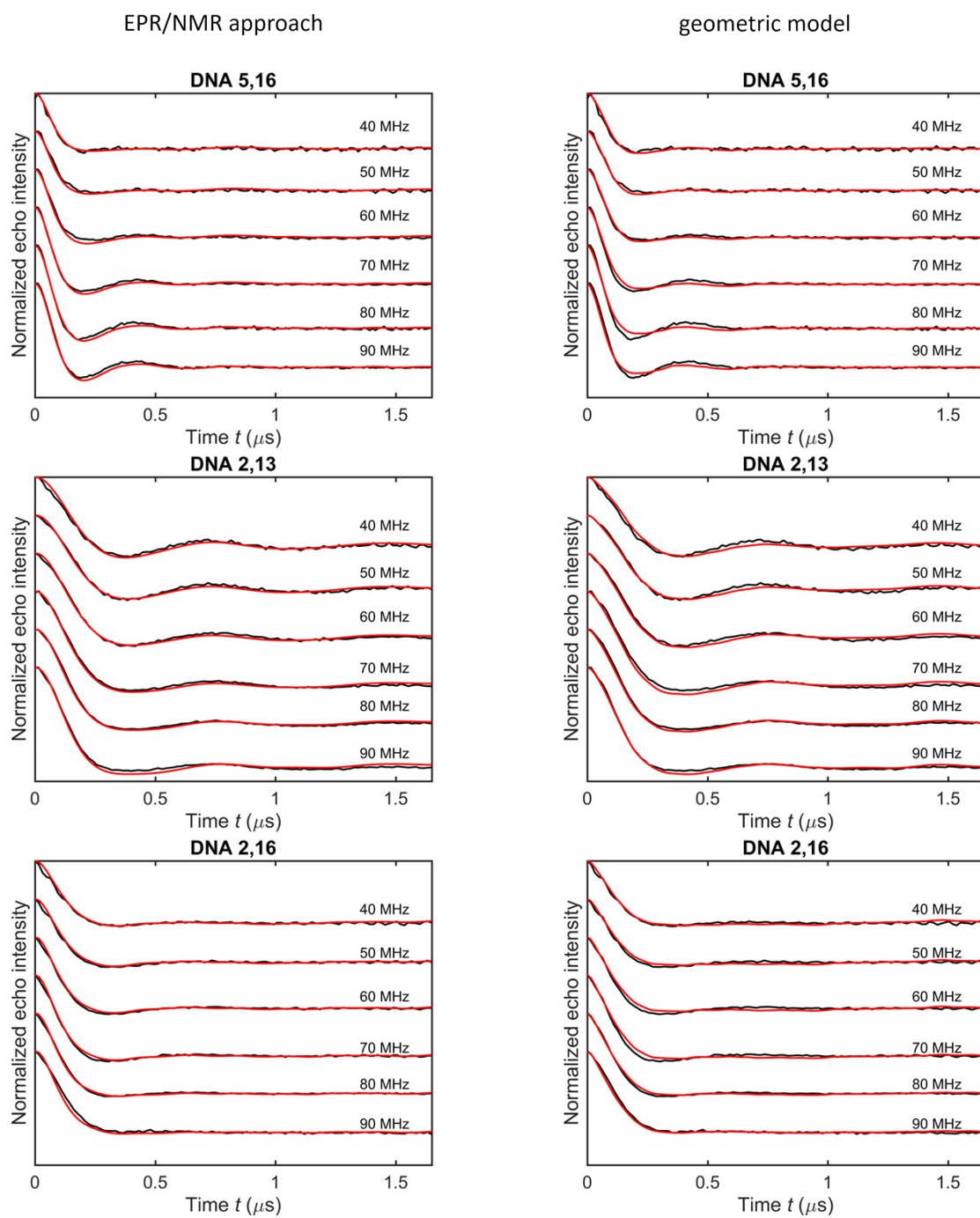


**Fig. S9** Experimental X-band (black) and fitted PELDOR time traces of all DNA samples. Left: Fit from the structures derived by NMR and PELDOR restraints shown without offset correction. Right: Fit from the geometrical model.

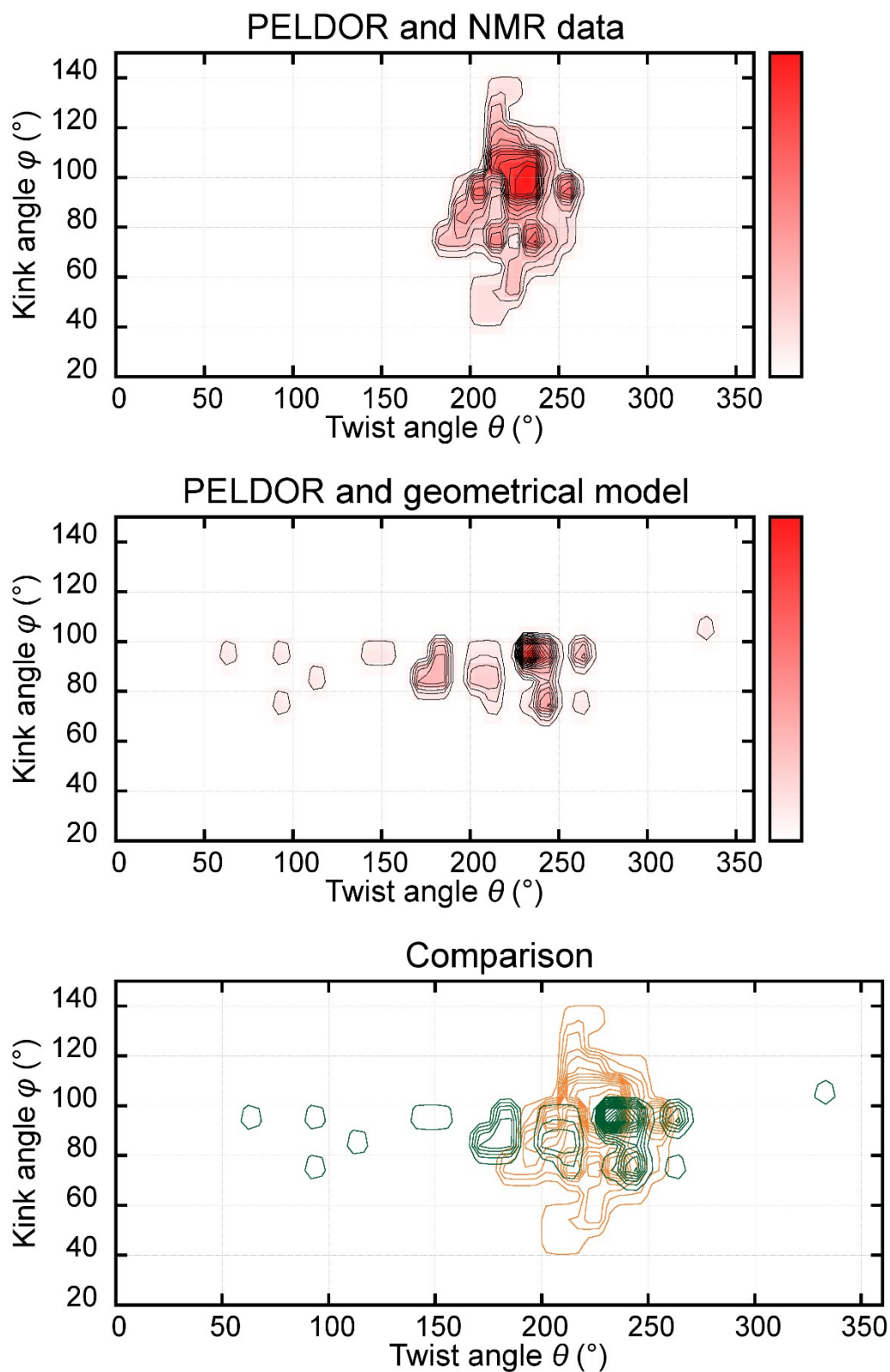


**Fig. S10** Density plot of twist angle against bend angle of the structures selected by the fit from the structures derived by NMR and PELDOR restraints (top) and from the geometrical model (middle) and both density plots for better comparison (bottom).

## 5.5 Calculation of the helix axis

For the calculation of the DNA helix axis, the principal component of the positions of the heavy atoms N2, N1 O6, N4, N3, O2, N1, N6, N3, and O4 (in PDB nomenclature) involved in base pairing hydrogen bonds are used. For stem 1 these atoms were selected from the bases 2–6 and 124–128 and for stem 2 from the bases 12–16 and 119–123 (leaving out the terminal base pairs). The second axis of the helix was set orthogonal to the helix axis using the reference atom C1' from (the arbitrary chosen) residue 4 for stem 1 and from residue 14 for stem 2, respectively. The calculation of the kink angle  $\varphi$  and the twist angle  $\theta$  were done as described by Wozniak *et al.*<sup>8</sup> Since the base sequence is not the same for the DNA helices, the twist angle  $\theta$  cannot be compared with the twist angles obtained by FRET. The phase of the  $\theta$  angle depends on an arbitrarily selected reference atom defining the x-axis of the axis system and thus is reliant on the base sequence of the considered structure (Fig. 5C).

## 5.6 Prediction of high-field PELDOR data

For validation of the EPR/NMR structural ensemble found by using the X-band frequencies data, we recorded PELDOR time traces at Q-band and G-band frequencies and predicted these data using the EPR/NMR structural ensemble (Fig. S11 and Fig. S12, respectively).

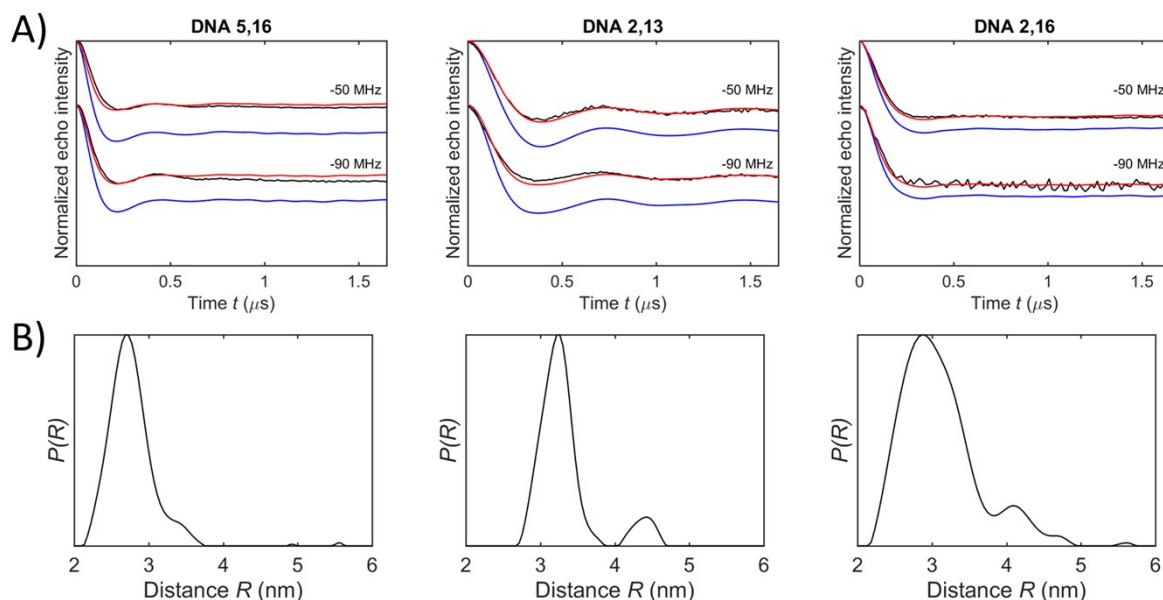


**Fig. S11** (A) Experimental Q-Band PELDOR time traces (black) and simulated Q-Band PELDOR time traces from the structures derived by NMR and PELDOR restraints of all DNA samples (blue). The modulation depth of the PELDOR traces of the simulation has been adjusted to the experimental trace for better comparison (red). (B) Distance distributions based on a Tikhonov regularization of the Q-band PELDOR data averaged over all measured frequency offsets  $\Delta\nu$ .

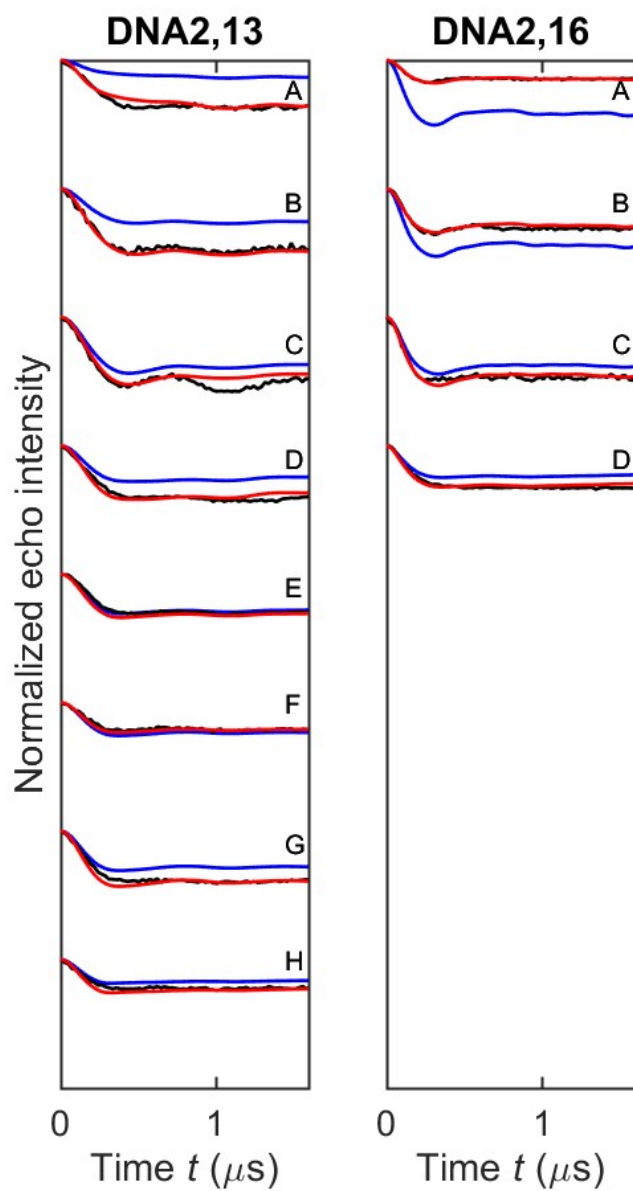


**Fig. S12** Experimental G-Band PELDOR time traces (black) and simulated G-Band PELDOR time traces from the structures derived by NMR and PELDOR restraints of **DNA2,13** and **DNA2,16** (blue). The modulation depth of the PELDOR traces of the simulation has been adjusted to the experimental trace for better comparison (red). The field positions A-H are marked in Figure S2C.

## 5.7 Simultaneous fit to all experimental PELDOR data

To test the accuracy of the results, we used simultaneously all our PELDOR time traces recorded at several magnetic field strengths (at X-, Q-, and G-band frequencies) for an overall fit. The reproducibility of the modulation depth at G-band frequencies is within 39-74% (Fig. S3). Therefore, the modulation depth was completely neglected during the fitting process. Due to the small modulation depth of time traces recorded at G-band frequencies (maximal 5%) in comparison to X-band (about 40%), or Q-band (about 20-30%) frequencies data, the deviation of experimental and simulated time traces could be large. Therefore, we consider the error function  $Err_n$  of the time traces recorded at G-band frequencies 20 times more than the time traces recorded at X- or G-band frequencies.



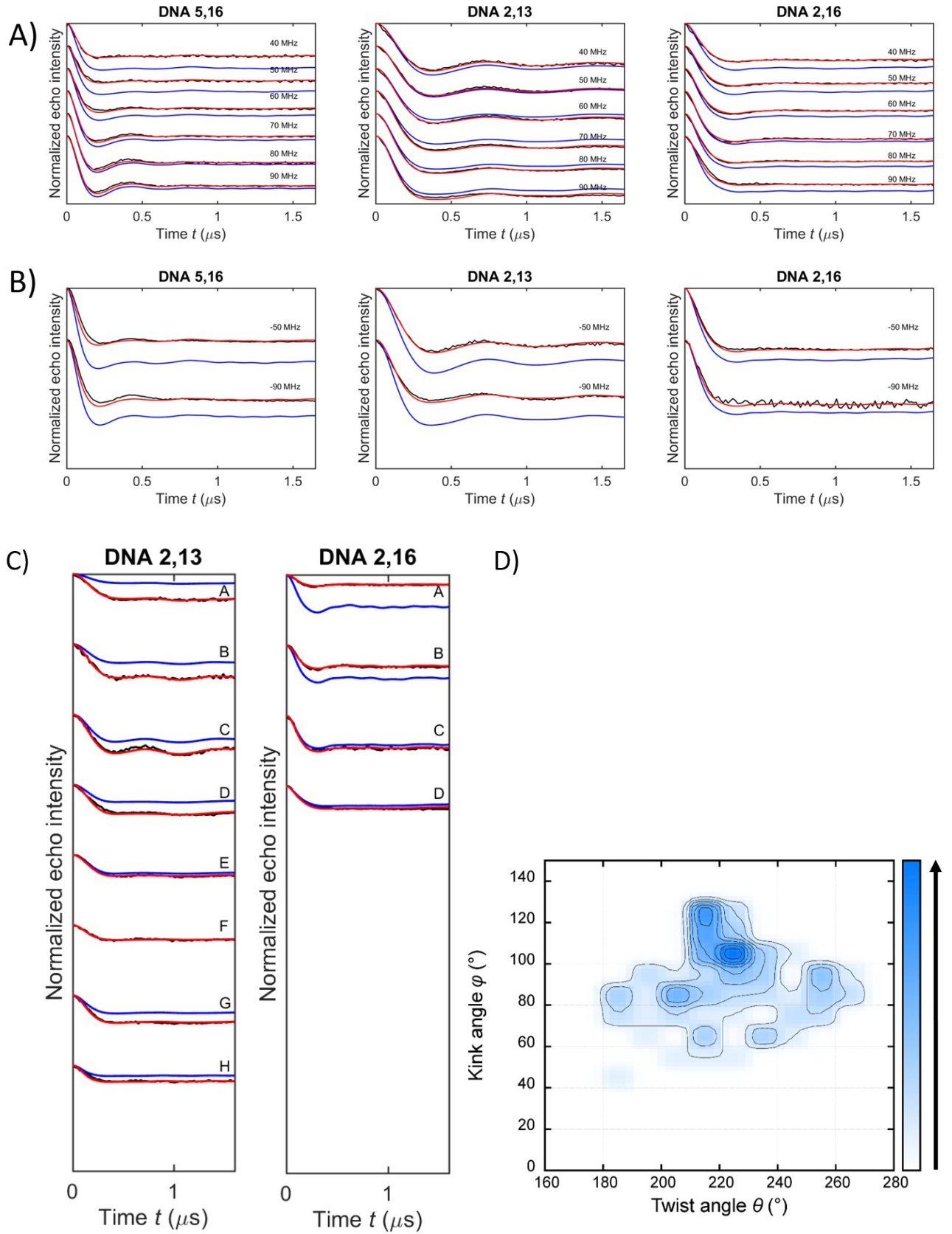


**Fig. S13** Experimental G-Band PELDOR time traces (black) and simulated G-Band PELDOR time traces from a simultaneous fit to all experimental data of **DNA5,16**, **DNA2,13** and **DNA2,16** (blue). The modulation depth of the PELDOR traces 2.0  $\mu\text{s}$  of the simulation has been adjusted to the experimental trace for better comparison (red). (A) X-band (B) Q-band (C) G-band. The field positions A-H are marked in Fig. S2C. (D) Density plot of twist angle against bend angle of the structures selected by a simultaneous fit to all experimental data recorded at multiple magnetic field strengths.

## 6 References

1. Godt, A.; Schulte, M.; Zimmermann, H.; Jeschke, G., How flexible are poly(para-phenyleneethynylene)s? *Angew. Chem.-Int. Edit.* **2006**, *45* (45), 7560-7564.
2. Prisner, T. F.; Marko, A.; Sigurdsson, S. T., Conformational dynamics of nucleic acid molecules studied by PELDOR spectroscopy with rigid spin labels. *J. Magn. Reson.* **2015**, *252*, 187-198.
3. Jeschke, G.; Chechik, V.; Ionita, P.; Godt, A.; Zimmermann, H.; Banham, J.; Timmel, C. R.; Hilger, D.; Jung, H., DeerAnalysis2006 - a comprehensive software package for analyzing pulsed ELDOR data. *Appl. Magn. Reson.* **2006**, *30* (3-4), 473-498.
4. Tikhonov, A. N., *Numerical Methods for the Solution of Ill-posed Problems*. Kluwer Academic Publishers: Dordrecht: Bosten, 1995.
5. Marko, A.; Prisner, T. F., An algorithm to analyze PELDOR data of rigid spin label pairs. *Phys. Chem. Chem. Phys.* **2013**, *15* (2), 619-627.
6. Marko, A.; Margraf, D.; Yu, H.; Mu, Y.; Stock, G.; Prisner, T., Molecular orientation studies by pulsed electron-electron double resonance experiments. *J. Chem. Phys.* **2009**, *130* (6), 064102-1-064102-9.
7. Endeward, B.; Marko, A.; Denysenkova, V. P.; Sigurdsson, S. T.; Prisner, T. F., Advanced EPR methods for studying conformational dynamics of nucleic acids. *Methods Enzymol.*, eds. Qin PZ, Warncke K **2015**, *564*, 403-425.
8. Woźniak, A. K.; Schröder, G. F.; Grubmüller, H.; Seidel, C. A. M.; Oesterhelt, F., Single-molecule FRET measures bends and kinks in DNA. *Proc. Natl. Acad. Sci. U. S. A.* **2008**, *105*, 18337-18342.